Research Article | Vol. 11, No. 6 / 1 June 2021 / Optical Materials Express 1643
Optical Materials EXPRESS

Method for inferring the mechanical strain of GaN-on-Si epitaxial layers using optical profilometry and finite element analysis

B. F. Spiridon,[1,*] M. Toon,[2] A. Hinz,[1] S. Ghosh,[1] S. M. Fairclough,[1] B. J. E. Guilhabert,[2] M. J. Strain,[2] I. M. Watson,[2] M. D. Dawson,[2] D. J. Wallis,[1,3] and R. A. Oliver[1]

[1]Department of Materials Science and Metallurgy, University of Cambridge, Cambridge CB3 0FS, UK
[2]Institute of Photonics, Department of Physics, University of Strathclyde, Glasgow G1 1RD, UK
[3]Centre for High Frequency Engineering, University of Cardiff, Cardiff CF24 3AA, UK
[*]bfs25@cam.ac.uk

Abstract: GaN-on-Si has become a useful fabrication route for many GaN devices and applications, but the mechanical stress incorporated throughout the material stack can impact the viability of this approach. The transfer printing of GaN membrane devices, a promising emerging technology, is most effective with flat membranes, but in practice many GaN structures released from their Si substrate are highly bowed due to the strain in the epitaxial nitride stack. Our approach uses the optical profiles of epitaxial wafers and membranes as inputs for inferring the mechanical strain state of the material by multi-variable numerical model fitting using COMSOL Multiphysics. This versatile, adaptable and scalable method was tested on samples from two GaN-on-Si wafers, revealing the relationship between built-in strain and material bow in principal-component fashion, returning 3–4×10^{-4} strain estimates for the AlGaN (compressive) and GaN (tensile) layers, and suggesting the occurrence of plastic deformation during transfer printing.

1. Introduction

3D integration of optoelectronic devices is an important future technology for applications in areas such as quantum dot in cavity, multi-layer photonic integrated circuits, flexible and advanced displays, and biosensors [1–3]. Transfer printing [1,4] is a particularly attractive method to achieve 3D integration, its key benefits including: the transfer of fully fabricated devices, the integration of multiple materials on a single target substrate, the opportunity to stack devices, and the lack of need for post-transfer material processing (when substrate removal is best avoided, especially in the case of multi-layer and multi-material assemblies).

GaN devices have shown superior and unique performance in optoelectronic and high-power devices compared with alternative semiconductor technologies, but GaN bulk substrates are still prohibitively expensive for the majority of applications and hetero-epitaxial growth of GaN on dissimilar substrates is therefore commonly employed [5–7].

The choice of Si as a substrate for GaN epitaxy is advantageous compared with alternatives, such as sapphire or SiC, as Si wafers benefit from wide availability, low cost, compatibility with existing processing lines [8] and relatively high thermal conductivity [9]. Furthermore, GaN-on-Si technology permits the use of Si micro-machining techniques for selectively removing substrate regions to create suspended nitride structures, including cantilevers [10], anchored chiplets [11], and membranes [12]. Such suspended GaN structures show interesting mechanical and thermal characteristics while inheriting many strengths of free-standing GaN, e.g. high

#418728 https://doi.org/10.1364/OME.418728
Journal © 2021 Received 4 Jan 2021; revised 24 Mar 2021; accepted 6 Apr 2021; published 7 May 2021

Optical Materials EXPRESS

break-down voltage [13]. A particular advantage of creating anchored GaN structures is the possibility of detaching and transfer-printing [14] them onto alternative hard [15] or flexible [16] substrates, simultaneously enabling their integration with other semiconductor modules [11].

The manufacturing and processing of GaN-on-Si wafers are, however, limited by several mechanical aspects. These are predominantly related to the significant mismatch between the crystal lattice parameters and thermal expansion coefficients of GaN and Si, resulting in large levels of tensile stress in the epitaxial material. Device-specific design features, such as thick buffer regions or highly-doped layers, can further magnify the mechanical stress developed within the epitaxial GaN-on-Si stack. The effects of the built-in mechanical stress are detrimental both at the material level (promoting the development and propagation of crystal defects) and from a processing perspective (bowed wafers cannot be accurately processed using standard optical lithography processes).

Stress-mitigation architectures have been designed to reduce the epitaxial wafer bow, by introducing compressive strain to compensate the significant tensile stresses arising on cooling aiming to achieve a net-zero stress in the epitaxial stack [17–19]. However, this approach is not necessarily suitable for GaN-on-Si material intended for transfer printing, where GaN membrane devices are defined by deep trenches covering the majority of their perimeter (except for designated anchor regions) and the underlying region of the Si substrate is removed by chemical etching, resulting in suspended GaN membrane devices as shown in Fig. 1.

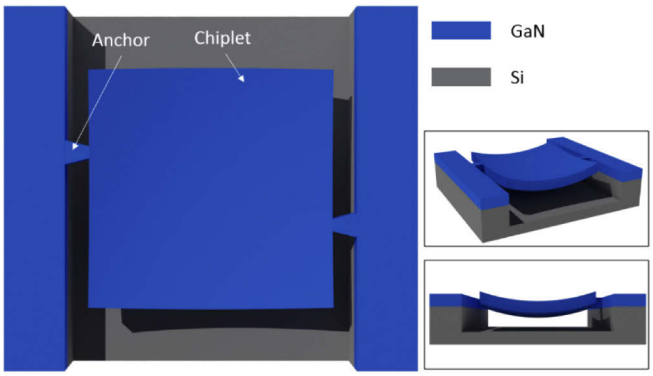

Fig. 1. Schematic structure of a GaN membrane device attached to its original Si substrate via anchors. Insets show additional 3D views of the same device, bowed by the complex mechanical stress built into its material

It was often observed [20–21] that such anchored GaN structures show a significant bow that persists or increases after the devices are released, posing a challenge for transfer printing and 3D integration, and supporting the case for robust design processes. While earlier transfer printing experiments circumvented this problem by using flexible receiver substrates [16] and intermediary adhesive layers [22–23], membrane devices can be transfer printed relying only on close-contact van der Waals-type adhesion forces [15,24–26]. This approach is advantageous e.g. for optical coupling [26] or heat dissipation [15], but is critically dependent on the device planarity, placing additional emphasis on the flatness of the GaN membranes.

Similar to wafer bow, membrane bow is a result of the built-in mechanical stress in the epitaxial material layers, but the type and magnitude of the bow at wafer and membrane level can be different. Understanding the relationship between wafer bow, membrane bow and the strain state of the epitaxy can provide insights which, for a particular epitaxial structure, may allow us to use wafer bow as an indicator of the expected behaviour of the membrane. To minimise the membrane bow, a balanced stress distribution must be ensured within the nitride epitaxy, ideally resulting in zero bending moment. This requirement is in addition to the low net-stress

Optical Materials EXPRESS

specification for low wafer bow, which still applies to the membrane-device transfer printing technology.

Achieving balanced stress-compensated stacks is the key to manufacturing flat wafers and flat membranes, receiving considerable attention in the context of transfer printing. Such studies require objective and detailed feedback regarding the stress in different parts of the epitaxial stack, but conventional methods of measuring stress in nitrides can be impractical or not sufficiently accurate. For example, it is hard to differentiate layers of similar composition in complex structures using conventional X-ray diffraction. Micro-Raman spectroscopy can be performed on such small samples, but it is also unsuitable for analysing complex material stacks. Similarly, transmission electron microscopy can be used to observe mechanical strain at the atomic level, but it is a localised, laborious, destructive and expensive technique, and the necessary sample processing can affect the original mechanical state.

We propose an alternative method that uses simple measurements of the wafer and membrane bow for inferring the mechanical state of the samples, including the strain of individual layers within complex material stacks. Bow measurement is comparatively more accessible and is routinely performed by non-contact in-situ optical methods during and/or immediately after the epitaxial wafer growth. Similarly, optical profilometry is a standard technique for assessing the profiles of wafers, dies and devices within cleanroom laboratories. In parallel, finite-element analysis (FEA) simulators are becoming more powerful, accurate, and accessible. Our work demonstrates the possibility of extracting information about the mechanical state of the nitride epitaxy by observing the wafer and membrane profiles and fitting an FEA model twin to recreate the experimental dataset. For validation, the full process was run on a set of two GaN-on-Si wafers with comparable stack structures, which provided complementary information about the mechanical stress developed in several regions of the epitaxial material.

2. Methods

Two GaN-on-Si LED wafers, Sample 1 and Sample 2, with structures as shown in Fig. 2, were investigated in this work, their growth being detailed in the Supplemental Document in Supplement 1. Their high epitaxial growth temperature, in the region of 1300 K, is an important source of mechanical stress upon cooldown due to thermal mismatch. The epitaxial structure of the LEDs is similar to the ones published in our previous works [27–28], being optimized to satisfy the electrical and stress-management requirements of GaN-on-Si LED technology to levels suitable for industrial production, hence having great relevance in the transfer printing context. Compared with Sample 1, Sample 2 contains an additional sub-monolayer SiNx dislocation blocking interlayer in the n-GaN epilayer. Such interlayers have been shown in the literature [29–31] to be effective in reducing the dislocation density in the overlying epitaxy, but their impact on the strain state of the material is poorly understood.

The curvature of the two sample wafers was monitored during the high-temperature epitaxial growth using an in-situ EpiCurve (Laytec, DE) system. These observations were complemented with ex-situ bow measurements at room temperature using a custom-made system for recording the final position of a laser beam reflected off different points on the wafer surface. The detection limit of this experimental bow measurement method is estimated theoretically to be around 3 µm for a 150 mm wafer, with errors of a similar order to this limit.

Each of the LED wafers was diced into 19×15 mm^2 pieces for processing, with the subsequent fabrication steps illustrated in Fig. 3(a) and further detailed in the Supplemental Document in Supplement 1. The mask used for the experiments defined square membranes with a side length of 100 µm, and a tapered anchor geometry with support and membrane contact widths of 10 and 5 µm respectively and a length of 10 µm. The anchors' design and their placement with a 30 µm relative offset along two opposite sides of the membrane device were previously observed to improve the transfer-printing yield and were used in this study to facilitate the integration

Optical Materials EXPRESS

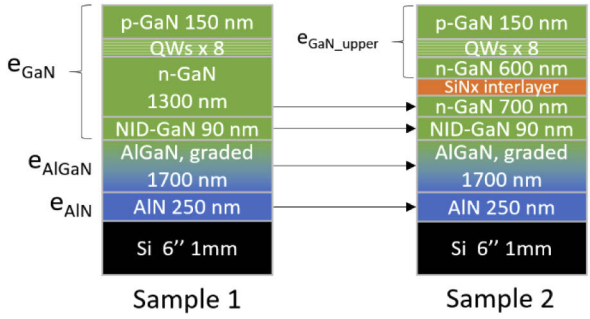

Fig. 2. Structure of the epitaxial GaN-on-Si material, with simplifying assumptions and parameter search strategy (discussed later): Sample 1 is segmented into three regions of distinct strains, constant along the growth direction; the best-fit values of these strains are transferred to Sample 2, which includes an additional strain level corresponding to the material region above the SiNx interlayer.

of our described method with the transfer-printing process. The mask pattern was aligned to give rows of membrane dies and intermediate support rails running parallel to Si <1-10>, as shown in Fig. 3(b). This orientation exposed Si surfaces prone to fast etching under the sides of membranes running in the perpendicular direction [16,32], enabling suspension of dies each held by two thin anchors, themselves also fully underetched.

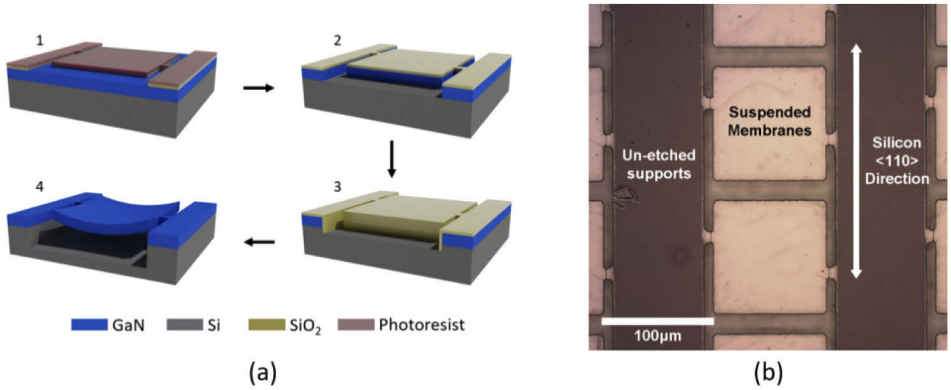

Fig. 3. The membrane device fabrication process (a): formation of the patterned silica hard-mask using RIE (1), ICP-RIE through the GaN device layers (2), second RIE for shallow Si etch, and PECVD deposition of silica sidewall protection (3), and final KOH

The membrane devices were individually transfer printed to a silicon receiver substrate using a reversible adhesion stamp comprised of elastomeric polydimethylsiloxane (PDMS) on a modified Nanoink dip-pen tool [11]. For each wafer, 3 membrane devices were printed onto a silicon substrate to allow for variations between devices to be assessed and an average membrane bow to be measured. Figure 4(a) shows a schematic of the printed devices. During printing, the membrane device is placed into contact with the substrate and pressure applied to ensure full contact between the surfaces. As the PDMS stamp is retracted, the device is released onto the substrate and the intrinsic membrane bow causes it to relax into a bowl-like shape. An optical microscope image, Fig. 4(b), of the released membrane device shows a circular interference pattern due to the air gap between the device bottom surface and the substrate. As the air gap

Optical Materials EXPRESS

increases in dimension away from the device contact area, the interference fringe spacing gives an indication of the membrane bow [33].

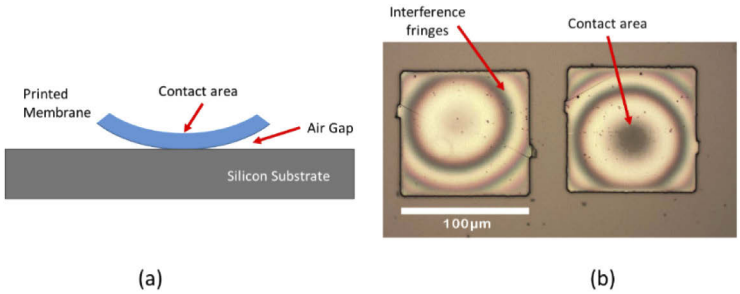

Fig. 4. (a) Schematic of the transfer printed membrane devices on Si illustrating the effect of membrane device bowing. (b) Optical microscope images of printed devices from different wafers (Left: Sample 1; Right: Sample 2)

To quantitatively assess the membrane bow, both as fabricated on their native wafer, and after transfer printing, the devices were measured using a Wyko NT1100 optical profiler instrument. To frame a single device, the 20x objective lens was combined with a 2x field of view lens. This allowed an accurate measurement of single devices with a depth resolution of a few nanometres.

The profiler image files were post-processed using Gwyddion [34] to extract the topology of the device top surface. Figure 5 shows extracted height maps of the membrane devices, both as fabricated (attached), and after transfer printing onto the recipient Si substrate. The steep profile changes over the peripheral ~10 μm of the attached membrane devices were assigned to optical interference between the surface of the attached device and the etch-well surface, as confirmed by the lack of such effect in the transfer-printed devices.

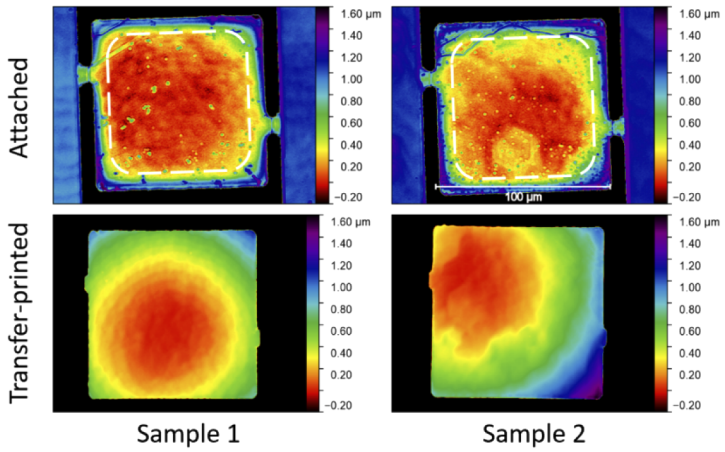

Fig. 5. Measured height maps of Samples 1 and 2 while attached and following transfer printing. The profiles of attached membrane devices are affected by an optical-interference measurement error in the peripheral regions marked by a dashed white line

COMSOL Multiphysics, a commercial FEA solver, was used to create a model of the GaN-on-Si material and to simulate the 3D profiles generated by built-in mechanical strain in different regions of the epitaxial stack. These strains, labelled as $e_{<\text{layer}>}$ and referenced to the unstrained lattice parameters of the bulk materials, were the independent variables of the model and were provided as inputs in the simulation of bow values as detailed below.

Optical Materials EXPRESS

A parameterised 3D geometry of the reduced wafer and membrane device was built, as shown in Fig. 6. The full 150 mm wafer diameter was reduced to 1 mm in the model to avoid unnecessary computational complexity, with the local radius of curvature (ROC) extracted from the reduced model and the equivalent bow then extrapolated to a 150 mm wafer equivalent.

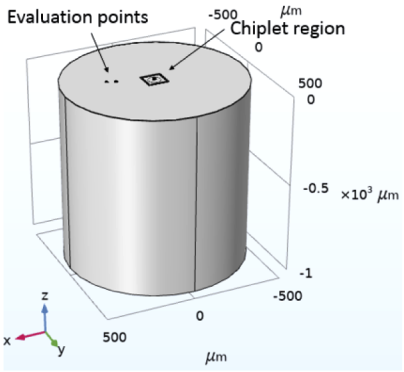

Fig. 6. 3D geometry of the reduced wafer and membrane device FEA model

The membrane device geometry and layer structure were reproduced in the model, as shown in Fig. 7, with the respective layer thicknesses defined as in Fig. 2, except for the SiNx interlayer, not included due to its sub-monolayer thickness.

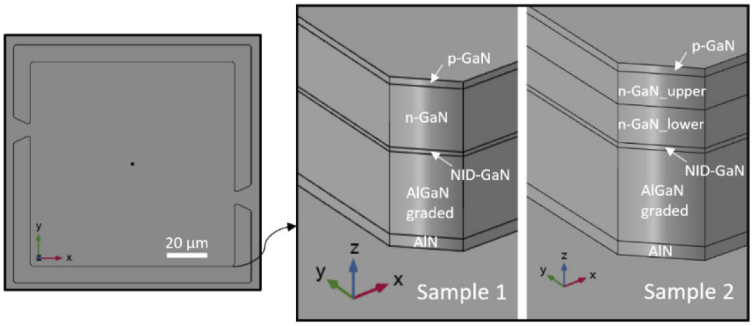

Fig. 7. Details of the membrane region of the model: (Left) plan view membrane device and anchors geometry and (Right) the structure of the epitaxial nitride layers of Samples 1 and 2

By solving for the mechanical deformation caused by the built-in strain, simulated profiles of the reduced wafer and membrane were obtained, as shown in Fig. 8. Three quantities of interest were extracted from these model solutions: the 150 mm-diameter full-wafer bow (B), the membrane bow along the anchors' direction (B_A), and the membrane bow along the diagonal away from the anchors (B_D). B is a commonly measured wafer property which was measured experimentally on full wafers and compared with the results of the reduced-size model by extrapolating the model bow to the equivalent bow of a 150 mm-diameter wafer. The direction along which B_A is measured is highly sensitive to the mechanical state of the substrate, while the direction along which B_D is measured yields the greatest membrane deformation, supporting greater experimental measurement accuracy. The membrane evaluation regions were limited to the central 70 μm to exclude any membrane edge effects. This choice of evaluation directions is supported by the direct effect of strain distribution within the layered stack on B_D and by the effect of the net mechanical state of the stack on B_A via the anchors. Together with the wafer

Optical Materials EXPRESS

bow, B, they are viable model fitting directions in the search for the original mechanical strains generating them. The independent-variable strains were considered the fitting parameters, i.e. degrees of freedom (DOF) of the problem.

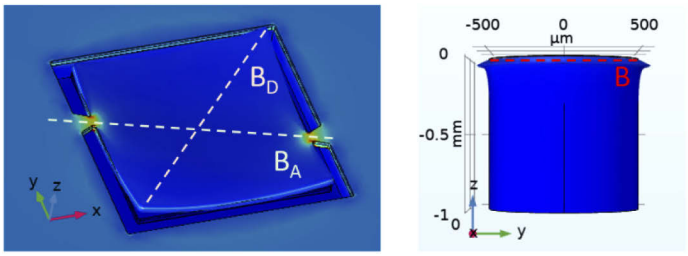

Fig. 8. Example of reduced wafer and membrane deformation (exaggerated) simulated using the FEA model

The FEA model results were compared against the experimentally recorded bow levels along the three directions of interest by calculating an equivalent 3D relative error, E_{rel}, as in Eq. (1) and using the result as the objective function for the model fitting process. In this process, the nominal values obtained experimentally were used, without including the experimental measurement errors. The fitting process relied on a multi-step exhaustive search method with progressively finer evaluation steps.

$$E_{rel} = \sqrt{\left(\frac{B_{FEA} - B_{exp}}{B_{exp}}\right)^2 + \left(\frac{B_{A,FEA} - B_{A,exp}}{B_{A,exp}}\right)^2 + \left(\frac{B_{D,FEA} - B_{D,exp}}{B_{D,exp}}\right)^2} \quad (1)$$

Given the three fitting dimensions, the search space dimensionality was reduced using simplifying assumptions, for a well-defined search problem. A multi-step approach was taken as shown in Fig. 2, where the system of built-in strain states in Sample 1 was reduced to three regions of constant strain and a further region was added when fitting Sample 2, taking into account the potential effect of the additional SiN_x layer on the strain state of the material grown subsequently. It is useful to note that, given the sub-monolayer thickness of the SiN_x region, its mechanical state does not significantly impact the overall mechanical state of the sample, hence the FEA model did not include this layer. This approach resulted in a 3-DOF problem for Sample 1 and an additional DOF for Sample 2. The direct transfer of best-fit strain levels from Sample 1 to Sample 2 is supported by the identical stack structures and epitaxial growth conditions between the two samples up to the SiN_x interlayer, while this additional DOF for Sample 2 is necessary as the SiN_x interlayer is expected to influence the mechanical state of the layer grown subsequently. Finally, the best-fit strain levels resulting from the two-step exhaustive searches were used to simulate the profile of free-standing GaN membrane devices and to compare them with the profiles of experimental transfer-printed devices, as observed using optical profilometry.

3. Results and discussion

Experimental optical profiles were recorded on sets of five attached and three transfer-printed membrane devices from each wafer (Sample 1 and Sample 2), extracting experimental values for the key parameters to be matched by the model, B_D and B_A, as summarised in Table 1 together with the associated standard errors and using the 'positive-concave, negative-convex' bow convention. The relative B_D:B_A magnitude indicates the degree of non-spherical bow for attached membranes, more pronounced in Sample 1 than in Sample 2. The B values previously recorded by wafer bow measurements are also included. While the wafer bow readings are relatively low, they are still significant compared with the results obtained from fresh Si wafers

Optical Materials EXPRESS

in the same batch for which the bow values were below the detection limit of the experimental method.

Table 1. Summary of optical bow measurements

Sample	SiN_x interlayer	B / µm	Step	B_D / µm	B_A / µm
1	No	−6 ± 2.7	Attached	0.15 ± 0.01	0.10 ± 0.01
			Transfer-printed	0.24 ± 0.03	0.24 ± 0.03
2	Yes	−8 ± 2.7	Attached	0.15 ± 0.03	0.16 ± 0.02
			Transfer-printed	0.22 ± 0.01	0.22 ± 0.01

The attached membrane devices of Sample 1 were simulated in a 3-DOF search space, with an initial coarse results series presented in Fig. 9. The labelled and colour-coded arrows in Fig. 9(a) indicate the principal directions of variation with changes in the strain states of the respective layers: e_{GaN} (red), e_{AlGaN} (blue), e_{AlN} (green). Each arrow's length is representative of the relative weight of each strained layer to the resulting bow state. While the large degree of correlation observed in Fig. 9(b) between B_A and B_D is undesirable for the parametric search as it reduces the accuracy of the results, the non-unity slope of the results locus in the B_A-B_D space indicates a non-spherical bow, as expected given the additional mechanical constraint introduced by the two support anchors.

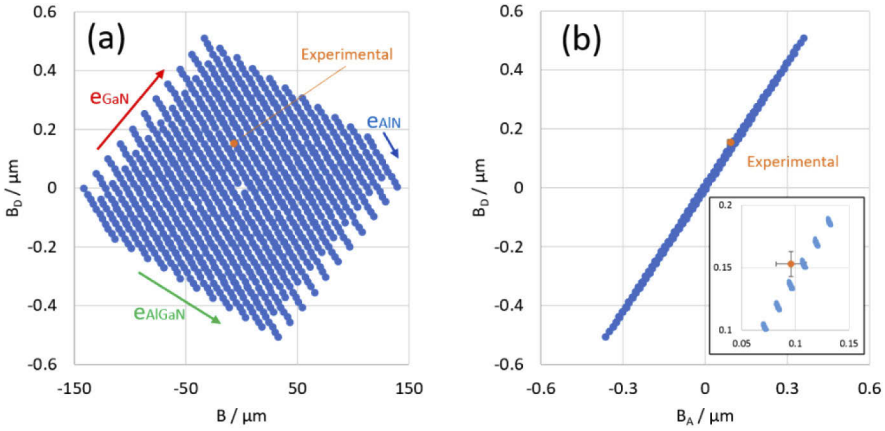

Fig. 9. 3D search space for attached membrane devices from Sample 1, generated by varying the three independent strain variables, e_{GaN} (red), e_{AlGaN} (green), and e_{AlN} (blue): variations and eigen-directions in the B-B_D space (a) and variations in the B_A-B_D space (b), with inset showing the region around the experimental results (standard-error bars)

These initial results showed that the membrane shape can be reproduced numerically by the FEA model, as judged by the proximity of experimental measurements to the numerical model results in Fig. 9. Further parametric searches with finer steps for the independent variables were performed until the best-fit results converged to approximately 8% relative error vs the experimental data. Since the B_A-B_D correlation results in a weaker problem definition, several good-fit combinations with relative errors in the range 8-10% were extracted for statistical analysis, shown in Fig. 10. These results indicate a tensile strain for the GaN region, compressive for the AlGaN layer, and slightly tensile for the AlN layer, albeit with a greater uncertainty.

It is important to note that the roughly equal-magnitude but opposite-sign strains of the lower AlGaN and upper GaN layers lead to both an essentially flat wafer, as their effects cancel at the wafer level, and bowed membranes, as a significant bending moment is developed at

Optical Materials EXPRESS

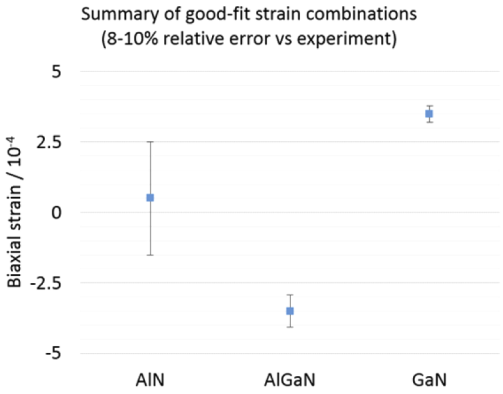

Fig. 10. Best-fit 3-DOF results for the attached membrane devices of Sample 1, with error bars indicating standard error

membrane-device scale. Consequently, flatter membranes can be achieved if the strain magnitude of both layers is reduced proportionally while maintaining a net-zero mechanical stress for flat wafers.

The best-fit strain values obtained from the attached membrane devices of Sample 1 were used in a second step, where the structures fabricated using Sample 2 were considered. An additional DOF was introduced as the equivalent strain in the GaN layers grown on top of the SiN_x interlayer and a 1-DOF exhaustive search was performed numerically, with the simulated results summarised in Fig. 11.

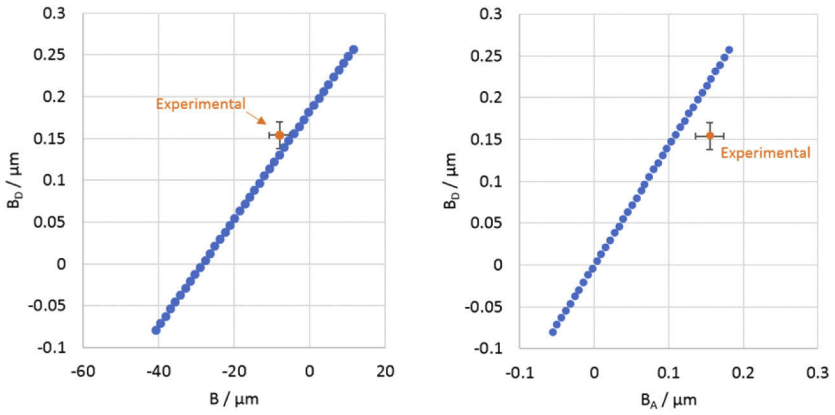

Fig. 11. Search space for attached membrane devices from Sample 2 (standard-error bars)

Regardless of the step size in the parametric step, the relative fit error was at least 40%, mainly attributed to the large deviation between simulated and experimental values in the B_D-B_A space, describing the membrane shape. A similar approach of considering several good-fit combinations with relative errors between 40% and 50% was taken, completing the statistical results presented in Fig. 12 with values for the GaN_upper strain independent variable.

The small reduction in mean strain estimate from GaN to GaN_upper suggests that the influence of the SiN_x interlayer on the strain state of the material is relatively small, supporting the use of such dislocation-reduction layers in GaN-on-Si epitaxy without substantially affecting their performance in a transfer printing context. Finally, the strain levels inferred from this method are

Optical Materials EXPRESS

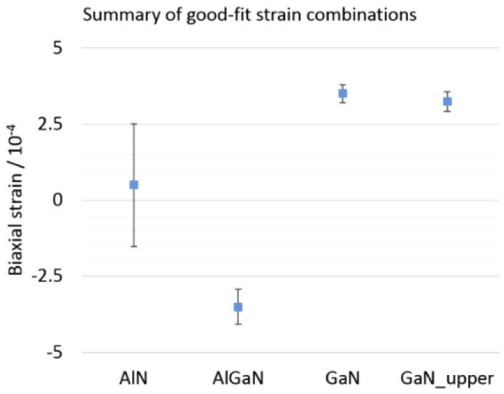

Fig. 12. Best-fit results for the attached membrane devices: AlN, AlGaN, GaN results from Sample 1 with relative error 8-10% and GaN_upper result from Sample 2 with relative error 40-50%; the error bars indicate standard error

plausible in the context of lattice and thermal mismatch, layer relaxation through defects, and material-specific mechanical limits before cracks start occurring.

To verify the last aspect related to mechanical limits, the distribution of mechanical stress along the crystal growth direction developed in the best-fit scenario was extracted from the full 3D mechanical model results, as shown in Fig. 13. These results confirm that the stress levels are below 200 MPa, values typical for GaN-on-Si material grown by MOCVD [35] and within the fracture toughness of the GaN epitaxial material, known to be in the region of 350 MPa [36].

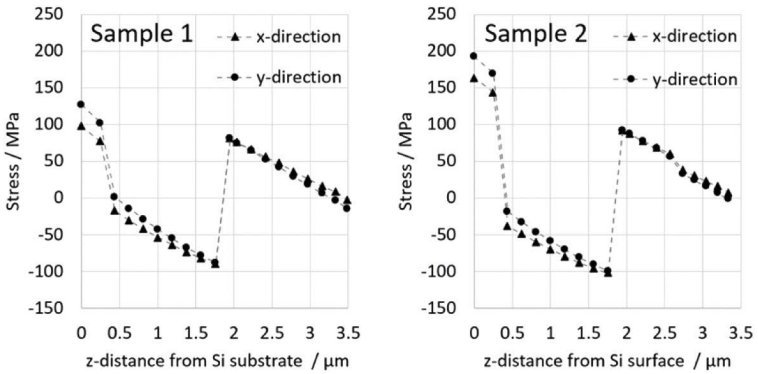

Fig. 13. Room-temperature mechanical in-plane stress levels at different levels along the wafer normal in the crystal growth direction, as extracted from the best-fit 3D FEA model results

It must be noted that, since significant levels of mechanical strain can be stored even in the initial Si substrates, several fresh Si wafers from the same batch were characterised ex-situ using the same laser bow measurement system and were found to be essentially flat, within the accuracy limits of the system. As a result, the model assumed initially relaxed Si substrates.

The best-fit mechanical strain levels inferred from the fitting of numerical simulation results to the experimental bow measurements were used to simulate the profile of free-standing GaN membrane devices detached from their original substrates. The numerical model results shown in Fig. 14 were compared with the experimental measurements, observing levels of bow between 22% (Sample 2) and 40% (Sample 1) lower than the experimental values.

Optical Materials EXPRESS

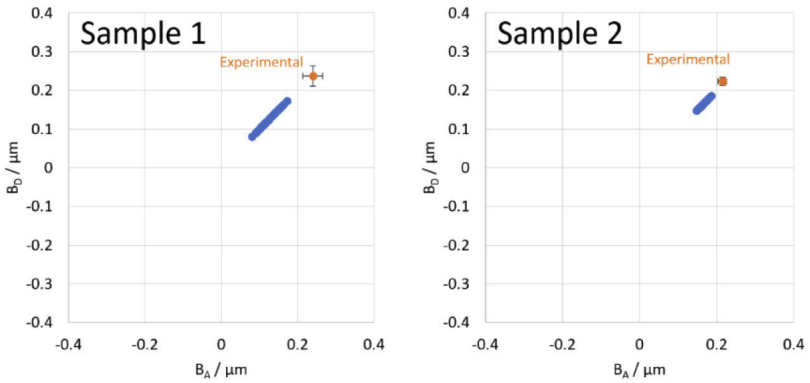

Fig. 14. Model strain estimates tested against experimental values for transfer-printed membrane devices, with error bars showing measurement standard error

The higher concave bow levels observed after transfer printing are unexpected, considering that the substrate was seen to apply a net compressive stress on the material. Similarly, the close-contact forces providing adhesion to the new substrate should only reduce the level of membrane bow. Instead, plastic deformation of the lower nitride layers, as a result of the downward forces applied by the printing head while breaking the anchors to release the membrane devices, is a plausible origin of the increased membrane bow. The results shown in Fig. 13 support the hypothesis of AlN cracking, as it experiences the greatest tensile stress. Additionally, the downward action of the print head applies more force to break the anchors and hence increases the tensile stress on the lower AlN layer, potentially inducing cracking and driving the system equilibrium towards a higher concave bow level. Given the unexpected result, the experimental verification of this hypothesis is an interesting topic for future research.

This FEA study of membrane devices provides additional insight over the mechanical state of nitride regions in two complex LED structures. Although several simplifying assumptions were necessary for a well-defined parametric fitting problem, this method expands the understanding of the GaN-on-Si epitaxial stacks beyond the level usually permitted by direct material characterisation. Its accuracy can be further increased with better problem definition. This can be achieved with simpler epitaxial structures and/or more independent experimental results. Nevertheless, this initial study demonstrated the viability of the technique using necessary simplifying assumptions on two complex LED structures, using a single test structure geometry. Further technique improvements also include simulating the formation and propagation of plastic defects and considering the weak close-contact adhesion forces in the case of transfer-printed membrane devices.

4. Conclusion

The use of GaN-on-Si material for transfer printing increases the importance of understanding and controlling the mechanical state of the material beyond the usual wafer-flatness criterion for optical lithography. The combined experimental and numerical technique described here infers the signs and levels of mechanical strain existing in such epitaxial structures by observing the wafer and membrane profiles and fitting these observations to a high-fidelity FEA model. This method is versatile and scalable to any levels of wafer and membrane bows, is adaptable to other materials and stack structures, and is easy to enhance with additional physics or geometry features.

The method was applied to two GaN-on-Si epitaxial wafers, returning valuable mechanical strain and stress estimates for the AlN, AlGaN and GaN regions of the epitaxial stack, revealing

Optical Materials EXPRESS

principal directions of wafer and membrane bow variation with the strain contained in each region, and highlighting the importance of mechanical stress balance in addition to net-zero mechanical stress. Specifically, the membrane bow was seen to depend on the imbalanced mechanical stress contrast developed in the nitride structure, which can be minimised through the general reduction of all built-in strain levels and by their more symmetrical placement along the growth direction.

The material analysis method described here can accelerate the research into GaN-on-Si stress management and the scale-up of the GaN-on-Si technology to larger wafer diameters, specifically 200 mm and beyond, by providing an accessible method of estimating the mechanical state of given epitaxial layers. Furthermore, this method can be directly integrated with complementary simulations (e.g. thermal or fluid dynamics) within the COMSOL Multiphysics FEA platform.

Funding. Engineering and Physical Sciences Research Council (EP/L015889/1, EP/N01202X/2, EP/R03480X/1); Cambridge Trust; Deutsche Forschungsgemeinschaft (HI 2141/1-1).

Acknowledgements. This work was part of the EPSRC Hetero-print project [EP/R03480X/1]. BFS is also a member of the EPSRC CDT Sensor Technologies and Applications [EP/L015889/1] and gratefully acknowledges the support from the Cambridge Commonwealth European and International Trust. AH would like to acknowledge funding for his position in the framework of a Research Fellowship by the Deutsche Forschungsgemeinschaft (DFG) under the grant number HI 2141/1-1. DJW acknowledges support from an EPSRC Manufacturing fellowship (EP/N01202X/2). The support offered by Mr. P. Hill in collecting the experimental optical profiler data is also gratefully acknowledged.

Disclosures. The authors declare no conflicts of interest.

Supplemental document. See Supplement 1 for supporting content.

References

1. A. Carlson, A. M. Bowen, Y. Huang, R. G. Nuzzo, and J. A. Rogers, "Transfer printing techniques for materials assembly and micro/nanodevice fabrication," Adv. Mater. **24**(39), 5284–5318 (2012).
2. J. McPhillimy, C. Klitis, P. Hill, S. May, B. Guilhabert, M. D. Dawson, M. Sorel, and M. J. Strain, "Towards 3D optical integration by micro-transfer printing of ultra-thin membrane devices," in *Proceedings of 2018 IEEE British and Irish Conference on Optics and Photonics (BICOP)*, London, UK (2018), pp. 1–4.
3. M. Choi, B. Jang, W. Lee, S. Lee, T. W. Kim, H.-J. Lee, J.-H. Kim, and J.-H. Ahn, "Stretchable active matrix inorganic light-emitting diode display enabled by overlay-aligned roll-transfer printing," Adv. Funct. Mater. **27**(11), 1606005 (2017).
4. B. Corbett, R. Loi, W. Zhou, D. Liu, and Z. Ma, "Transfer print techniques for heterogeneous integration of photonic components," Prog. Quantum Electron. **52**, 1–17 (2017).
5. H. Amano, Y. Baines, E. Beam, M. Borga, T. Bouchet, P. R. Chalker, M. Charles, K. J. Chen, N. Chowdhury, R. Chu, C. De Santi, M. M. De Souza, S. Decoutere, L. Di Cioccio, B. Eckardt, T. Egawa, P. Fay, J. J. Freedsman, L. Guido, O. Häberlen, G. Haynes, T. Heckel, D. Hemakumara, P. Houston, J. Hu, M. Hua, Q. Huang, A. Huang, S. Jiang, H. Kawai, D. Kinzer, M. Kuball, A. Kumar, K. B. Lee, X. Li, D. Marcon, M. März, R. McCarthy, G. Meneghesso, M. Meneghini, E. Morvan, A. Nakajima, E. M. S. Narayanan, S. Oliver, T. Palacios, D. Piedra, M. Plissonnier, R. Reddy, M. Sun, I. Thayne, N. Trivellin, V. Unni, M. J. Uren, M. Van Hove, D. J. Wallis, J. Wang, J. Xie, S. Yagi, S. Yang, C. Youtsey, R. Yu, E. Zanoni, S. Zeltner, and Y. Zhang, "The 2018 GaN power electronics roadmap," J. Phys. D: Appl. Phys. **51**(16), 163001 (2018).
6. B. Gill, *III-Nitride Semiconductors and their Modern Devices* (Oxford University Press, 2013).
7. D. Zhu, D. J. Wallis, and C. J. Humphreys, "Prospects of III-nitride optoelectronics grown on Si," Rep. Prog. Phys. **76**(10), 106501 (2013).
8. D. Marcon, B. De Jaeger, S. Halder, N. Vranckx, G. Mannaert, M. Van Hove, and S. Decoutere, "Manufacturing challenges of GaN-on-Si HEMTs in a 200 mm CMOS Fab," IEEE Trans. Semicond. Manuf. **26**(3), 361–367 (2013).
9. J. W. Johnson, E. L. Piner, A. Vescan, R. Therrien, P. Rajagopal, J. C. Roberts, J. D. Brown, S. Singhal, and K. J. Linthicum, "12 W/mm AlGaN-GaN HFETs on silicon substrates," IEEE Electron Device Lett. **25**(7), 459–461 (2004).
10. S. Gorman, D. Gajula, S. Kim, and G. Koley, "Impact of volatile organic compound exposure on electrical breakdown in GaN dual channel microcantilevers," Appl. Phys. Lett. **114**(11), 114103 (2019).
11. J. F. C. Carreira, A. D. Griffiths, E. Xie, B. J. E. Guilhabert, J. Herrnsdorf, R. K. Henderson, E. Gu, M. J. Strain, and M. D. Dawson, "Direct integration of micro-LEDs and a SPAD detector on a silicon CMOS chip for data communications and time-of-flight ranging," Opt. Express **28**(5), 6909–6917 (2020).
12. A. S. Yalamarthy, H. So, M. Muñoz Rojo, A. J. Suria, X. Xu, E. Pop, and D. G. Senesky, "Tuning electrical and thermal transport in AlGaN/GaN heterostructures via buffer layer engineering," Adv. Funct. Mater. **28**(22), 1705823 (2018).
13. P. Srivastava, J. Das, D. Visalli, M. Van Hove, P. E. Malinowski, D. Marcon, S. Lenci, K. Geens, K. Cheng, M. Leys, S. Decoutere, R. P. Mertens, and G. Borghs, "Record breakdown voltage (2200 V) of GaN DHFETs on Si with 2-μm buffer thickness by local substrate removal," IEEE Electron Device Lett. **32**(1), 30–32 (2011).

Optical Materials EXPRESS

14. S. Kim, J. Wu, A. Carlson, S. H. Jin, A. Kovalsky, P. Glass, Z. Liu, N. Ahmed, S. L. Elgan, W. Chen, P. M. Ferreira, M. Sitti, Y. Huang, and J. A. Rogers, "Microstructured elastomeric surfaces with reversible adhesion and examples of their use in deterministic assembly by transfer printing," Proc. Natl. Acad. Sci. **107**(40), 17095–17100 (2010).
15. A. J. Trindade, B. Guilhabert, E. Y. Xie, R. Ferreira, J. J. D. McKendry, D. Zhu, N. Laurand, E. Gu, D. J. Wallis, I. M. Watson, C. J. Humphreys, and M. D. Dawson, "Heterogeneous integration of gallium nitride light-emitting diodes on diamond and silica by transfer printing," Opt. Express **23**(7), 9329–9338 (2015).
16. H. Kim, E. Brueckner, J. Song, Y. Li, S. Kim, C. Lu, J. Sulkin, K. Choquette, Y. Huang, R. G. Nuzzo, and J. A. Rogers, "Unusual strategies for using indium gallium nitride grown on silicon (111) for solid-state lighting," Proc. Natl. Acad. Sci. **108**(25), 10072–10077 (2011).
17. H. Ishikawa, G.-Y. Zhao, N. Nakada, T. Egawa, T. Jimbo, and M. Umeno, "High-Quality GaN on Si substrate using AlGaN/AlN Intermediate Layer," Phys. Status Solidi A **176**(1), 599–603 (1999).
18. A. Able, W. Wegscheider, K. Engl, and J. Zweck, "Growth of crack-free GaN on Si(111) with graded AlGaN buffer layers," J. Cryst. Growth **276**(3-4), 415–418 (2005).
19. E. Feltin, B. Beaumont, M. Laugt, and P. de Mierry, "Stress control in GaN grown on silicon (111) by metalorganic vapor phase epitaxy," Appl. Phys. Lett. **79**(20), 3230–3232 (2001).
20. Y. Zhang, S.-W. Ryu, C. Yerino, B. Leung, Q. Sun, Q. Song, H. Cao, and J. Han, "A conductivity-based selective etching for next generation GaN devices," Phys. Status Solidi B **247**(7), 1713–1716 (2010).
21. M. Rais-Zadeh, V. J. Gokhale, A. Ansari, M. Faucher, D. Théron, Y. Cordier, and L. Buchaillot, "Gallium Nitride as an Electromechanical Material," J. Microelectromechanical Syst. **23**(6), 1252–1271 (2014).
22. I. Christiaens, G. Roelkens, K. De Mesel, D. Van Thourhout, and R. Baets, "Thin-film devices fabricated with benzocyclobutene adhesive wafer bonding," J. Lightwave Technol. **23**(2), 517–523 (2005).
23. X. Sheng, C. Robert, S. Wang, G. Pakeltis, B. Corbett, and J. A. Rogers, "Transfer printing of fully formed thin-film microscale GaAs lasers on silicon with a thermally conductive interface material," Laser Photonics Rev. **9**(4), L17–L22 (2015).
24. E. Yablonovitch, D. M. Hwang, T. J. Gmitter, L. T. Florez, and J. P. Harbison, "Van der Waals bonding of GaAs epitaxial liftoff films onto arbitrary substrates," Appl. Phys. Lett. **56**(24), 2419–2421 (1990).
25. B. Guilhabert, J. McPhillimy, S. May, C. Klitis, M. D. Dawson, M. Sorel, and M. J. Strain, "Hybrid integration of an evanescently coupled AlGaAs microdisk resonator with a silicon waveguide by nanoscale-accuracy transfer printing," Opt. Lett. **43**(20), 4883–4886 (2018).
26. J. McPhillimy, B. Guilhabert, C. Klitis, M. D. Dawson, M. Sorel, and M. J. Strain, "High accuracy transfer printing of single-mode membrane silicon photonic devices," Opt. Express **26**(13), 16679–16688 (2018).
27. D. Zhu, C. McAleese, K. K. McLaughlin, M. Häberlen, C. O. Salcianu, E. J. Thrush, M. J. Kappers, W. A. Phillips, P. Lane, D. J. Wallis, T. Martin, M. Astles, S. Thomas, A. Pakes, M. Heuken, and C. J. Humphreys, "GaN-based LEDs grown on 6-inch diameter Si (111) substrates by MOVPE," Proc. SPIE **7231**, 723118 (2009).
28. D. Zhu, C. McAleese, M. Häberlen, C. Salcianu, T. Thrush, M. Kappers, A. Phillips, P. Lane, M. Kane, D. Wallis, T. Martin, M. Astles, N. Hylton, P. Dawson, and C. Humphreys, "Efficiency measurement of GaN-based quantum well and light-emitting diode structures grown on silicon substrates," J. Appl. Phys. **109**(1), 014502 (2011).
29. M. Haeberlen, D. Zhu, C. McAleese, M. J. Kappers, and C. J. Humphreys, "Dislocation reduction in MOVPE grown GaN layers on (111)Si using SiNx and AlGaN layers," J. Phys. Conf. Ser. **209**, 012017 (2010).
30. M. J. Kappers, M. A. Moram, Y. Zhang, M. E. Vickers, Z. H. Barber, and C. J. Humphreys, "Interlayer methods for reducing the dislocation density in gallium nitride," Phys. B Condens. Matter **401-402**, 296–301 (2007).
31. F. Yun, Y.-T. Moon, Y. Fu, K. Zhu, Ü. Ozgür, and H. Morkoç, "Efficacy of single and double SiNx interlayers on defect reduction in GaN overlayers grown by organometallic vapor-phase epitaxy," J. Appl. Phys. **98**(12), 123502 (2005).
32. R. E. Oosterbroek, J. W. Berenschot, H. V. Jansen, A. J. Nijdam, G. Pandraud, A. van den Berg, and M. C. Elwenspoek, "Etching methodologies in <111>-oriented silicon wafers," J. Microelectromechanical Syst. **9**(3), 390–398 (2000).
33. P. Hill, E. Gu, M. D. Dawson, and M. J. Strain, "Thin film diamond membranes bonded on-demand with SOI ring resonators," Diamond Relat. Mater. **88**, 215–221 (2018).
34. D. Nečas and P. Klapetek, "Gwyddion: an open-source software for SPM data analysis," Open Phys. **10**(1), 181–188 (2012).
35. H. Marchand, L. Zhao, N. Zhang, B. Moran, R. Coffie, U. K. Mishra, J. S. Speck, S. P. DenBaars, and J. A. Freitas, "Metalorganic chemical vapor deposition of GaN on Si(111): Stress control and application to field-effect transistors," J. Appl. Phys. **89**(12), 7846–7851 (2001).
36. T. Zimmermann, M. Neuburger, P. Benkart, F. J. Hernandez-Guillen, C. Pietzka, M. Kunze, I. Daumiller, A. Dadgar, A. Krost, and E. Kohn, "Piezoelectric GaN sensor structures," IEEE Electron Device Lett. **27**(5), 309–312 (2006).